Using discrete multi-physics for detailed exploration of hydrodynamics in an in vitro colon system

Alexiadis, A.; Stamatopoulos, K.; Wen, W.; Batchelor, H. K.; Bakalis, S.; Barigou, M.; Simmons, M. J H

DOI:
10.1016/j.compbiomed.2017.01.003

Document Version
Peer reviewed version

Citation for published version (Harvard):
Alexiadis, A, Stamatopoulos, K, Wen, W, Batchelor, HK, Bakalis, S, Barigou, M & Simmons, MJH 2017, 'Using discrete multi-physics for detailed exploration of hydrodynamics in an in vitro colon system', *Computers in Biology and Medicine*, vol. 81, pp. 188-198. https://doi.org/10.1016/j.compbiomed.2017.01.003

Using discrete multi-physics for detailed exploration of hydrodynamics in an in vitro colon system

A. Alexiadis[a1], K. Stamatopoulos[a], W. Wen[a], H. K. Batchelor[b], S. Bakalis[a], M. Barigou[a], M. J. H. Simmons[a].

[a] School of Chemical Engineering, University of Birmingham, Birmingham, Edgbaston, Birmingham, B15 2TT United Kingdom.

[b] College of Medical and Dental Sciences, University of Birmingham, Birmingham, Edgbaston, Birmingham, B15 2TT United Kingdom

Abstract

We developed a mathematical model that describes the motion of viscous fluids in the partially-filled colon caused by the periodic contractions of flexible walls (peristalsis). In-vitro data are used to validate the model. The model is then used to identify two fundamental mechanisms of mass transport: the surfing mode and the pouring mode. The first mechanism is faster, but only involves the surface of the liquid. The second mechanism causes deeper mixing, and appears to be the main transport mechanism. Based on the gained understanding, we propose a series of measures that can improve the reliability of in-vitro models. The tracer in PET-like experiments, in particular, should not be injected in the first pocket, and its viscosity should be as close as possible to that of the fluid. If these conditions are not met, the dynamics of the tracer and the fluid diverge, compromising the accuracy of the in-vitro data.

Keywords: mathematical modelling; peristalsis; smoothed particle hydrodynamics; fluid dynamics; intestine; fluid-structure interaction.

1. Introduction

The colon is the least researched GI region in terms of drug absorption, yet for orally administered formulations, colonic absorption represents the only real opportunity to increase the interval between doses. The extent and importance of colonic absorption are, however, difficult to predict due to the highly variable transit time and permeability; lack of knowledge on fluid flow and a lack of in vivo predictive models. A model that predicts the concentration of drug at the surface of the colon is likely to correlate to drug performance as this is the site of absorption for systemically absorbed drugs or the site of action for many drugs for local targeting within the colon.

However, the mechanism of mass transfer in the colon under the effect of peristaltic motion is not well understood, especially in the case of partially-filled intestine. In-vivo experiments are expensive and time consuming (Hur et al. 2011), while in-vitro models typically require a compromise between technical complexities and biological features (Guerra et al. 2012).

Nowadays, mathematical modeling and computer simulations have become a valuable investigation tool in medicine. *In-silico* models, in fact, are increasingly supporting traditional in-vivo and in-vitro models to achieve a better understanding of many physiological and biomechanics phenomena. Computational Fluid Dynamics (CFD), in particular, has proven itself a powerful tool in the study of transport phenomena in the GI tract (see Misra and Pandey 2006 for a review). In the majority of works, however, the external walls are considered rigid, and the fluid is not propelled by the contraction of flexible membranes as in the real case. One of the few exceptions is Sinnott at al. (2012) that couples Smoothed Particle Hydrodynamics (SPH) with a Mass-and-Spring representation of the membrane to study the hydrodynamics in flexible pipes subjected to peristalsis.

All these models refer to the completely filled intestine. However, most of the time the intestine is only partially filled (Schiller et al. 2005) and models for this case are not available. In this paper, we use an approach similar to Sinnott at al. (2012) to describe the hydrodynamics in partially-filled flexible-ducts with peristalsis. In order to validate the model, we use data from an in-vitro colon model developed at the University of Birmingham.

[1] Corresponding author: a.alexiadis@bham.ac.uk

The model is then used to address the following research question: “How can we improve the reliability of in-vitro models of the colon?” Considering that we know very little of the actual colon peristalsis, this seems a daunting task. Therefore, we attacked the problem from an unconventional angle. Instead of looking at the similarities between the in-vitro model and the real colon, we focused on the aspects that the in-vitro model *cannot* capture. Specifically, by investigating the main features of the flow, we identify the features of the in-vitro model with the highest probability of being different from the real case. Based on this knowledge, we suggest possible changes to improve the current experimental practice.

2. Modelling

2.1 Modelling approach

To simulate the motion of both the internal fluids and the external membrane, we use a *Discrete Multi-Physics* approach based on the so-called Discrete Multi-hybrid System (DMHS). The DMHS links different discrete (i.e. particle based) modelling techniques in order to reach results not attainable with each technique separately. This method has been successfully tested for both solid-liquid flows (Alexiadis 2014, Alexiadis 2015a, Alexiadis 2015b) and fluid-structure interaction (Ariane et al. 2016). In this study, Smoothed Particle Hydrodynamics (SPH) is used to simulate the fluid, and Coarse Grained Molecular Dynamics (CGMD) the membrane. Since both these methods are particle-based, their coupling is simple and direct. This is an advantage over continuum-discrete coupling, which require computational interfaces to connect the continuum and the discrete solvers as discussed in Alexiadis et al. (2013), Alexiadis et al. (2014), and Alexiadis et al. (2015).

In this study, models for solid contact/collision (e.g. the Discrete Element Method), or for fluctuating hydrodynamics (e.g. Dissipative Particle Dynamics) are not necessary; consequently, the coupling is limited to SPH (liquid phase) and CGMD (solid phase). The modelling approach, therefore, resembles that of Sinnott at al. (2012), with the difference that we use both bond and angle potentials to model the membrane, whereas Sinnott et al. (2012) only uses bonds.

A brief introduction to SPH and CGMD is given in the Appendix, together with the approach used to couple these two models. Specific details and other applications of the DMHS can be found in Alexiadis (2014), Alexiadis (2015a), Alexiadis (2015b) and Ariane et al. (2016). In previous DMHS publications, there is an interchangeable use of the terms CGMD and Mass-Spring Model (MSM). This depends on the fact that these articles cover different scales. Articles dealing with microscopic scales use CGMD, whereas articles dealing with macroscopic scales use MSM. Mathematically, however, these two techniques are equivalent. In the main text, we prefer MSM, which is more consistent with the scale under investigation. In the Appendix, we use CGMD, which is more consistent with the original DMHS formulation.

2.2 Geometry

The geometry investigated here does not refer directly the colon, but to an *in-vitro* tube of the intestine developed at the University of Birmingham and based on the anatomy of the adult colon (Stamatopoulos et al. 2016).

Figure 1a shows a schematic representation of the experimental Dynamic Colon Model (DCM). The tube consists of ten segments with 20 cm total length and diameter 5 cm. Inflation and deflation of the membrane of each segment is achieved by controlling the back and forward displacements of a syringe using a stepper motor. By synchronizing the oscillations of the segments, an antegrade wave with speed of 2 cm s^{-1} is produced. This speed value represents the velocity observed in proximal colon of healthy humans based on manometric measurements (Dinning et al., 2014). At the end of the tube, a rigid siphon was placed which represents the hepatic flexure and keeps the fluids inside the DCM tube during propulsive waves generated by the wall motion. The tube was placed horizontally

in accordance to the normal reclining position of patients during manometric, scintigraphy and MRI procedures.

The 2D geometry used in the simulations is described in Figure 1b, the channel is divided in $N+1$ pockets (segments), of roughly elliptic shape, representing the intestine's *haustra*. We number these pockets from 0 to N; their length is b, and L is the level of fluid in the partially-filled channel with the pockets in the relaxed state. The horizontal position of the pockets is measured from the centre of the first pocket. Therefore, the first pocket is located at $x_0 = 0$, the second at $x_1 = b$, and the k^{th} pocket at $x_k = kb$.
The fluid moves from one pocket to the other due to the contraction of the membrane (Figure 1c). When it reaches the last segment, it overflows and moves out of the computational domain. In the calculations, we assume that all the fluid particles that exit the system are ideally collected in an hypothetical $(N+1)^{th}$ pocket located at $x_{N+1} = (N+1)b$. Particles in the $(N+1)^{th}$ pocket are deleted reducing the number of the computational particles over time.

The fluid is divided into SPH particles, whose number depends on the level of liquid in the channel (see Appendix). The membrane is modelled with 5,250 MSM particles distributed in three layers. Figure 1b also shows the springs-and-hinges structure (only two layers are shown) used to model the membrane. Details concerning the bond (springs) and angle (hinges) potentials are in the Appendix. Since this study only deals with the partially filled intestine; the motion of the upper membrane is ignored. Figure 1d shows a snapshot of the simulation; a wall bounds the first pocket on the left, while an overflow allows the fluid to exit the channel from the right. The role of the white particles is discussed in Section 2.4.

2.3 Peristaltic contraction

Muscles contract in sequence to produce a peristaltic wave, which propels the digesting food along the intestine. There are various types of contractions in the intestine and, in general, their exact dynamics is unknown. In the simulations, therefore, we focus on the peristaltic wave used in the artificial colon model, which mimics the so-called *high-amplitude propagating sequences* (Dinning et al. 2008). In Section 4.5, we investigate a different contraction wave.

In the experimental apparatus (Figure 1a), the segments move with a predetermined pattern that produces a mass propagation wave. In the computer simulations, we recreate this pattern through the following steps (Figure 2).

- At time t=0, all pockets are in their relaxed state, no force is applied.
- At time t_w, a force in the upper direction is applied to the first pocket and a downwards force to the second pocket.
- At time $2t_w$, the upwards force is maintained to keep the membrane of the first pocket at its highest location, while the downwards force is released so that the second pocket gradually returns to its equilibrium configuration.
- At time $3t_w$, the force on the first pocket is released, an upwards force is applied to the second pocket, and a downward force to the third.

The configuration at time $3t_w$, therefore, is the same of time t_w only shifted by one pocket. The configuration at time $4t_w$ is the same of that at time $2t_w$, only shifted by one pocket and so on. In this way, all the pockets progressively contracts and expand recreating the peristaltic wave used in the experiments. Figure 3 shows the propagation of the wave as result of this sequence of contractions and expansions. Table 1 illustrates the same concept in matrix notation; 1 indicates an upwards force applied to a particular pocket at a specific time interval, -1 indicates a downwards force. As Table 1 indicates, every 2 rows, the same pattern is shifted by one column and repeated.

We name each time interval t_w a *sub-period* of the wave. If we look at each column in Table 1 (grey areas), we see that, during a peristaltic wave, each pocket has a recurrent dynamics of the type

[-1, 0, 1, 1]. This dynamics last for four sub-periods and we call it *haustrum-period*. The contraction of all the N+1 pockets takes T_w=(2N+5)t_w, which is the *peristaltic-period*. After the whole wave is completed, the process restarts with a new peristaltic wave. In this work, each simulation is composed of 10 peristaltic waves.

The peristaltic velocity is defined as the ratio between T_w and the total length of the channel (N+1)b

$$V_w = \frac{(N+1)b}{T_w}. \tag{1}$$

2.4 Preliminaries and dimensionless analysis

In order to study mass propagation in the channel, we introduce *tracking particles* in the first pocket at the beginning of the simulation. These are SPH particles with exactly the same properties of those in the rest of the flow. We can distinguish them only because they have a different colour in the snapshots (Figure 3) and, therefore, we can track their trajectories during the simulation.

In order to study the propagation of mass within the system, we introduce the concept of *front penetration* (x_F) and *front velocity* (u_F). If the ordinate of particle i at time t is x_i, we define the front penetration as

$$x_F = \sum_{i=0}^{n_P} \frac{x_i}{n_P}, \tag{2}$$

which represents the average location of all the tracking particles. The front velocity u_F should be the time derivative of the front position x_F. However, since the peristaltic wave causes discontinuous front propagation, we define it on the basis of the front penetration at the end of one peristaltic period, i.e.

$$u_F = \frac{x_F(t = T_w)}{T_w}. \tag{3}$$

In general, we want to calculate u_F given the variables L (liquid level, see Figure 1b), h (membrane uplift, Figure 1c), ν (kinematic viscosity) and V_w (speed of the peristaltic wave, eq. 1); b (distance between pockets, Figure 1b), on the other hand, is considered constant (2 cm). According to the Buckingham π theorem, there are four fundamental dimensionless groups: Re (Reynolds number), Ga (Galileo number), Fr (Froude number) and Λ (geometric ratio) defined as follows

$$\mathrm{Re} = \frac{bu_F}{\nu},\ \mathrm{Ga} = \frac{h^3 g}{\nu^2},\ \mathrm{Fr} = \frac{V_w}{\sqrt{gh}},\ \Lambda = \frac{h}{L}. \tag{4}$$

The forces that generate the peristaltic wave and the elastic properties of the membrane are not directly accounted in these four dimensionless groups. However, they are already comprised in the variable h that indicates the maximum height at which the membrane is lifted by the applied force F. In the simulation, we calibrate F to achieve a final membrane displacement (h) of around 1 cm, as in the experiments. In this study, b is considered constant and therefore only four dimensionless groups are required. If b were variable a fifth group (e.g. b/L) would be necessary.

3. Results

3.1 Simulations

There are two types of parameter required for the simulations: model parameters and simulation parameters. The first group consists of internal parameters used by the SPH and MSM solvers; the

second refers to the operative conditions. This Section focuses on the second group (i.e. L, h, ν and V_w); the other parameters can be found in the Appendix.

We carried out a large number of simulations (104 in total) that, approximately, cover the operative conditions of the experiments (Stamatopoulos et al. 2015); ν was varied between $0.5 \cdot 10^{-6}$ and $500 \cdot 10^{-6}$ m^2 s^{-1}, V_w between 4.3 cm s^{-1} and 26.1 cm s^{-1}, L between 0.46 and 1.6 cm, h between 0.88 and 1.16 cm. Each simulation lasted for ten peristaltic waves. With respect to the fundamental dimensionless groups identified in Section 2.4, the simulations cover the following ranges: Ga = $23-5 \cdot 10^7$, Fr = 0.023−0.15, Λ = 0.5−1.9, which result in Re $2 \cdot 10^{-3}$−40.

The resulting equations were solved with the help of the LAMMPS (Plimpton 1995) open source code. LAMMPS is a molecular dynamics code, but it is possible to implement it in such a way to combine bond, angle and SPH (Ganzenmüller et al. 2011) potentials together. The calculations were run on the BlueBear cluster computer located at the University of Birmingham using four 64-bit 2.2 GHz Intel Sandy Bridge E5-2660 cores with 32 GB of memory. Each simulation took approximately 48 hours to complete.

3.2 Validation

In order to validate the model, we compare the simulation results with experimental data (Stamatopoulos et al. 2016). Positron Emission Tomography (PET) system developed in University of Birmingham was used to assess the mixing process within the DCM tube under anterograde waves. The DCM tube was half-filled and placed between the two positron cameras and 1 mL of radiolabelled water was injected in the first segment. Ten anterograde waves, with 10 s time delay between them, were applied. The duration of each frame is 1 s. Concentration distribution of the radioactive solution in grayscale values vs distance along the x axis in pixels size (0.25 mm) are plotted in Figure 4. The grayscale value of each pixel is the mean of the vertical pixel intensities within the tube at each point.

We compare the number of tracking particles in the simulations with the grayscale of the radioactive tracer in PET experiments at approximately the same conditions and after the same number of peristaltic periods (Figure 4).

In general, the comparison shows a good agreement between experimental data and calculations. The only exception occurs in the first pocket, which shows considerably higher concentrations in the simulations. This is probably due to the fact that the simulations and the experiments have two very different methodologies to 'initialize' the tracking fluid in the first pocket. In the simulations, we simply attribute all the particles of the pocket to the tracking set. In the experiments, the radioactive compound is injected from above into the first pocket that is already filled with liquid. If we normalize the first segment (N0 in Figure 4) to match the simulation with the experiments and rescale the distribution, however, the results are very similar as indicated by Figure 4.

3.3 Method for calculating the front velocity (u_F) from the simulations

Figure 5a shows how the front penetration x_F (the average position of the white particles) varies with time for the case of L= 0.46 cm $\nu = 2 \cdot 10^{-6}$ m^2 s^{-1}, V_w = 1.45 cm s^{-1}. The propagation has an irregular profile. The tracking particles, driven by the peristaltic wave, move in a pulse-like manner. The simulations were carried out for ten waves, and we can distinguish ten pulses in Figure 5. A simple way to calculate the front velocity u_F is to determine the linear least-square approximation of x_F (dotted lines in Figure 5): the slope of this line provides u_F. In certain cases, however, linear fitting is not satisfactory. Figure 5b, for instance, shows the simulation for L = 0.81 cm $\nu = 1.6 \cdot 10^{-6}$ m^2 s^{-1}, V_w = 1.45 cm s^{-1}. Linear fitting is adequate only for the first 80 s. After 80 s, a significant amount of fluid has left the channel and the level L has decreased. Generally, we observe that front propagation is faster at lower L. Figure 5b graphically depicts this series of events. After 80 s, L decreases because fluid exits the channel and, consequently, the slope increases. However, when the level decreases below a certain threshold, the fluid in each pocket remains trapped in isolated pools. In this case, the

velocity propagation drops. Figure 5c (L= 0.46 cm $\nu = 10^{-6}$ m^2 s^{-1}, V_w= 1.45 cm s^{-1}) illustrates this: after 40 s, u_F gradually decreases due to the formation of separated liquid pools.

In the next Sections, we calculate u_F from the simulations. When the slope is not constant, we use the initial slope as illustrated in Figure 5b and 5c. We adopted this convection because in the real intestine new material enters to replace what is lost. We do not expect, therefore, the level of liquid to change as in the simulations.

4. Discussion

Observation (e.g. Figure 3) of both simulations and experimental data (Stamatopoulos et al. 2016) shows that there are at least two simultaneous modes of front propagation. In the first case, which we called *pouring mode*, the peristaltic wave pushes the fluid from one pocket to the next causing a certain level of mixing. Each time the tracking particles move to a new pocket, a certain number of them are left behind and remain in the previous pocket. In the second mode, which we called *surfing mode*, the motion occurs on the surface without appreciable mixing with the bulk. In this case, the tracking particles can move longer distances by surfing over the surface of the liquid. However, the surfing mode can be affected by backflow that occurs during the lifting of the membrane. The interaction of surfing and backflow originates a third sub-mode that we named *ineffective surfing*. This Section discusses these three possibilities in detail.

4.1 Pouring Mode

The pouring mode arises when some mixing occurs within each pocket. Initially, all the tracking particles n_P are located in the first pocket. At the end of a haustrum-period, a fraction α of particles has moved from the first to the second pocket. This fraction is the result of both forward motion, caused by the contraction of the first membrane, and backflow, caused by the contraction of the third membrane (Figure 6).

During the next haustrum-period, a fraction α of particles leaves the second pocket and goes into the third pocket. Assuming that α remains constant, the particles in the third pocket are now $\alpha^2 n_P$ and those in the second pocket $(1-\alpha)\alpha n_P$. By following the same logic, we can infer the number of particles in the k^{th} pocket at the end of the j^{th} period. As an example, Table 2 shows how the number of particles changes in the first 4 pockets during the first 3 haustrum-periods.

On the basis of these considerations, we can derive the front position at the end of the peristaltic wave for the pouring mode

$$x_P = \sum_{k=0}^{N} \frac{bk(1-\alpha)\alpha^k n_P}{n_P}. \qquad (5)$$

In eq. 5, instead of using x_i to calculate the average position of the tracking particles (as done in eq. 2), we approximate the position of all the particles contained in the k^{th} pocket with the position kb of the pocket.

The series in eq. 5 has solution

$$x_P = b\frac{\alpha - (N+1)\alpha^{N+1} + N\alpha^{N+2}}{(1-\alpha)}, \qquad (6)$$

which, since α<1 and N is a relatively large number (here N=9), can be further simplified to

$$x_P \cong \frac{\alpha}{1-\alpha} b\,, \tag{7}$$

and finally

$$u_P = \frac{\alpha}{1-\alpha}\frac{b}{T_w} = \frac{\alpha}{1-\alpha}\frac{V_W}{(N+1)}\ . \tag{8}$$

4.2 Surfing mode

In this case, the tracking particles from the first pocket slide above the surface of the second, and stop only after they surpass the centre of the pocket (Figure 7).

In this way, during the following haustrum-period, the flow from the second pocket pushes the tracking particles further forwards. In the most extreme case, all the particles αn_P, which left the first pocket initially, are pushed further to the third pocket. From the third pocket, they are pushed to the fourth and so on. One period after the other, the particles keep surfing forwards in synchrony with the peristaltic wave. At the end of the wave, the position of the front is simply the average between the particles remained in the first pocket (positions x_0), and those that exit the system after surfing over the entire channel surface (positions x_{N+1}).

$$x_S = \frac{(1-\alpha)n_P x_0 + \alpha n_P x_{N+1}}{n_P}\,. \tag{9}$$

Equation 9 can be further simplified since $x_0 = 0$ and $x_{N+1} = (N+1)b$ (see Section 2.2). Introducing these values in eq. 9, we obtain

$$x_S \cong \alpha b(N+1)\,. \tag{10}$$

The front velocity is calculated by dividing eq. 10 by T_w

$$u_S = \frac{\alpha b(N+1)}{T_w} = \alpha V_W\,. \tag{11}$$

The fast front propagation of the surfing mode should be considered as an idealized case. If we assume a typical value of α=0.1 and N=9, as in the simulations, u_S is around one order of magnitude larger than u_P.

4.3 Ineffective surfing mode

The surfing mode bases its effectiveness on the fact that, at each period, the front surpasses the centreline of the next pocket. In this way, it is ideally located to catch the next wave and advance further. However, if the fluid is viscous, it does not always move far enough to reach the centreline. Therefore, when the membrane of the next pocket goes up, the tracking particles are caught into the backflow and, instead of advancing, they are pushed back to the previous pocket (Figure 8). This is also an idealized situation, where the particles go back and forth from the first to the second pocket without actually propagating along the channel. As a consequence, the front propagation for ineffective surfing u_I is negligible.

We can establish a general criterion to determine whether, given a certain fluid viscosity, the surfing mode is effective or ineffective. We start from the Navier-Stokes equation where only the transient and the viscous terms are considered.

$$\frac{Du}{Dt} - \nu \frac{d^2u}{dx^2} = 0\,, \tag{12}$$

where D indicates the material derivative. Based on the order of magnitude, we can estimate the time τ that a fluid particle with initial velocity u will take to rest

$$\frac{u}{\tau} \sim \nu \frac{u}{b^2}\,, \tag{13}$$

and therefore

$$\tau \sim \frac{b^2}{\nu}\ . \tag{14}$$

During this time, the front propagation advances of Δx_F under the effect of u_F and, therefore,

$$\Delta x_F \sim \tau u_F. \tag{15}$$

Combining eq. 14 and 15, we obtain

$$\Delta x_F \sim \frac{u_F b^2}{\nu}. \tag{16}$$

As explained above, surfing is effective only when the propagation pulse brings the tracking particles beyond the centreline of the next pocket ($\Delta x_F > b$, from the centreline of the first pocket to the centreline of the second pocket). If this does not happen, the backflow brings the particles back to the initial pocket. This implies that the surfing mode is effective only if

$$\frac{u_F b^2}{\nu} > b\,, \tag{17}$$

which, using the definition of Reynolds number of eq. 4, can be rewritten as Re > 1. When this condition is met, ineffective surfing not only contrasts the effect of the surfing mode, but it can also act against the pouring mode as illustrated in Figure 3.

4.4 Which is the dominant mode?

The propagation velocities u_P, u_S and u_I refer to idealized situations. We expect the actual front velocity u_F to be a combination of the modes discussed above. The simulations show that the dominant mode is the pouring mode, and generally u_P is of the same order of magnitude of the final front velocity u_F. In combination with the pouring mode, surfing can be either effective or ineffective; in the first case $u_F > u_P$, in the second $u_F < u_P$. Figure 9 compares the Reynolds number calculated using the actual velocity u_F (Re in eq. 4) with that calculated using u_P (substitute u_P with u_F in eq. 4).

Data close to the diagonal are those where $u_F \sim u_P$ and the pouring mode is dominant. In general, u_P provides a good approximation of u_F for Re > 1. In some simulations u_F is higher than u_P (due to effective surfing), but this only happens at low viscosities ($\nu \leq 2 \cdot 10^{-6}$ m^2 s^{-1}). However, for Re < 1, u_F becomes gradually smaller than u_P, which is consistent with our proposed criterion for ineffective surfing.

4.5 Effect of the type of peristaltic wave

The actual shape of the peristaltic wave in the intestine is unknown and the available data show large clinical variability (e.g. Cook et al. 2000; Dinning et al. 2008; Dinning et al. 2014). In the previous sections, we looked at various wave speeds V_w, but the shape of the wave was always the same (the one used in the experiments). In this section, we investigate a different shape to assess the impact of the wave shape on mass propagation. Table 3 shows the matrix representation of this new wave. In the old wave, the contraction of each membrane section was maintained for two periods, in the new wave it is maintained for five periods (see also Figure 10).

We repeated with the new wave the same 104 simulations carried out for the old wave. In the new wave, at any given time, more membrane segments are contracted (Figure 10). This confers a higher "squeezing power" to the new wave that propels more fluid forwards.

Figure 11 illustrate this point. In the new wave, after 40 s, we observe a (least-square) slope increase, which indicates a decrease in the level of liquid, as discussed in Figure 5. After 100 s, the system reaches a plateau, which indicates the formation of isolated pools.

In the old wave, on the contrary, the level does not change much since the profile maintains a (least square) stable slope. However, if we only look at the first 40 s when the fluid level is comparable, the slope is similar for both cases. Since we calculate the front velocity u_F based on the initial slope (see Section 3.3), its value does not change significantly between the old and the new wave.

It may look like a contradiction that the new wave drives more fluid out of the channel but, at the same time, the front velocity remains roughly the same. The explanation of this apparent contradiction depends on the fact that all the tracking particles are initially located in the first pocket. The net flow rate in the first pocket is lower than in the other pockets because (using Figure 12 as reference) the first pocket has only one neighbour on the right, while, on the left, is constrained by a wall. Therefore, there is no inflow from the left that pushes the tracking particles forward, but there is backflow from the right that moves back some of the particles that had left the pocket.

To further clarify this point, we use a second type of tracking particles (red particles in Figure 12). These particles initially are located in the fifth pocket. We compare the propagation of red and white particles between the old and the new wave. Concerning the white particles, there is no big difference between the two waves in Figure 12, confirming what we already know from Figure 11. Concerning the red particles, the number of particles leaving the fifth pocket with the new wave is almost ten times larger. We observe, in particular, that the surfing layer is thicker. This implies that the surfing mode is more significant in the fifth pocket than in the first pocket and, therefore, these two pockets are not hydrodynamically equivalent.

4.6 Difference of viscosity between fluid and tracer

We run several simulations where the viscosities of the main fluid (blue particles) and the tracer (white particles) are different. In particular, we consider $\nu = 500 \cdot 10^{-6}$ m^2 s^{-1} for the main fluid and $\nu = 10^{-6}$ m^2 s^{-1} for the tracer. This reproduces the experimental situation where a syringe is used to inject the tracer into the main fluid from above forming a sort of cavity-like pool

Figure 13 compares the dynamics when the tracer and the fluid have the same viscosity ($500 \cdot 10^{-6}$ m^2 s^{-1}), and when the tracer viscosity is decreased 500 times. Counterintuitively, the tracer, instead of propagating faster because it is less viscous, propagates slower. This depends on the fact that mixing is hindered in fluids with highly different viscosities (Regner et al. 2008). Consequently, the pool tends to remain segregated from the main flow and propagation, after three peristaltic waves, is almost negligible.

5. Conclusions

In this paper, we devised a computational model for peristaltic motion including flexible boundaries and partially-filled intestine. This fills a gap in the literature. Previous works, in fact, only dealt with the completely filled intestine, but for most of the time the intestine is only partially filled.

The mathematical model is able to describe the main hydrodynamic events in a bio-relevant colonic model developed at the University of Birmingham (Stamatopoulos et al. 2016). Based on the improved understanding of the colon dynamics, we can suggest two factors that must be taken into account during the design and running of in-vitro experiments.

a) Particular attention should be given to the viscosity of the tracer. Reliable results can only be achieved if the viscosity of the tracer and that of the fluid are very close. If this does not occur, the tracer segregates from the main flow, compromising the reliability of the measurements. This has also relevance when looking at drug delivery systems to ensure that the viscosity of the drug-containing particles is well characterised.

b) The first pocket has a different dynamics from the rest of the colon. As a consequence, the tracer should not be injected in the first pocket unless we are exclusively interested in the dynamics of the caecum. It requires many peristaltic waves, to move a significant quantity of tracer from the first to the central pockets. Thus, if the goal is to investigate the motion in a generic haustrum, it is not efficient to inject the tracer into the first pocket.

The results presented in this paper have also implications for both medical research and pharmaceutical applications.

It is not clear why in human studies a clear correlation between in-vivo scintigraphy and manometric data cannot be found (e.g. Cook at al. 2000; Dining et al. 2008). Besides obvious technical difficulties, we can explain this on purely hydrodynamic grounds. In this study, we identified three major modes of mass propagation in the colon: pouring, surfing and ineffective surfing. Each scintigraphy frame produces an image of the tracer distribution, but it does not tell us the sequence of modes that each fluid element has followed to reach its final position. On the contrary, manometric measurements provide the sequence of modes experienced by individual pressure sensors, but not the overall picture. Based on these considerations, we anticipate that a clear correlation between scintigraphy and manometric data can be established only if large numbers of pressure sensors are used at the same time.

Concerning pharmaceutical applications, our simulations suggest how the dissolution of enteric coatings should be carefully calibrated. Understandably, the release of the drug should not occur too late, otherwise there would not be enough time for the drug to be absorbed. However, if the release occurs in the first pockets, where the dynamics is slow, the drug will not propagate effectively in the intestine, resulting in high local concentrations and potential side effects.

Appendix

A1. Smoothed particle hydrodynamics (SPH)

Smoothed particle hydrodynamics is an approximation method for the numerical calculation of partial differential equations. It is a mesh-free method where the solution is calculated on a set of pseudo-particles characterized by their own mass, velocity and density. The starting point is the identity

$$f(\mathbf{r}) = \iiint f(\mathbf{r}')\delta(\mathbf{r}-\mathbf{r}')\mathbf{dr}', \qquad \text{(A1)}$$

where $f(\mathbf{r})$ is a function of the position vector $\mathbf{r}$ and $\delta(\mathbf{r})$ the delta function. In the SPH framework, the delta function is approximated by a smoothing kernel W that satisfies

$$\lim_{h\to 0} W(\mathbf{r},h) = \delta(\mathbf{r}). \qquad \text{(A2)}$$

This brings to

$$f(\mathbf{r}) \approx \iiint f(\mathbf{r}')W(\mathbf{r}-\mathbf{r}',h)\mathbf{dr}', \quad \text{(A3)}$$

which, approximated over a series of pseudo-particles of mass $m = \rho(\mathbf{r})\mathbf{dr}$, gives

$$f(\mathbf{r}) \approx \sum_i \frac{m_i}{\rho_i} f(\mathbf{r}_i)W(\mathbf{r}-\mathbf{r}_i,h), \quad \text{(A4)}$$

where $f(\mathbf{r_i})$, m_i and ρ_i are the mass and density of the i^{th} particle, and i ranges over all particles within the smoothing kernel (i.e. $|\mathbf{r}-\mathbf{r}_i| < h$). We can use eq. A4 for the velocity $\mathbf{v}$ and the pressure P to approximate the Navier-Stokes equation (Liu and Liu 2003)

$$m_i \frac{d\mathbf{v}_i}{dt} = \sum_j m_i m_j \left(\frac{P_i}{\rho_i^2} + \frac{P_j}{\rho_j^2} + \Pi_{i,j}\right)\nabla_j W_{i,j} + \mathbf{f}_i, \quad \text{(A5)}$$

where the i and j subscripts refer, respectively, to particle i and particle j, $W_{i,j}$ means $W(\mathbf{r_j}\text{-}\mathbf{r_i}, h)$, ∇_j denotes the gradient with respect to r_j, $\mathbf{f}_i$ is the body force, and $\Pi_{i,j}$ the viscous stress tensor (here we use $\Pi_{i,j}$ from Morris et al. 1997). The velocities of the fluid particles are updated by means of eq. A5, while the density by means of the continuity equation

$$\frac{d\rho_i}{dt} = \sum_j m_j \mathbf{v}_{i,j}\nabla_j W_{i,j}, \quad \text{(A6)}$$

where $\mathbf{v}_{i,j} = \mathbf{v}_i - \mathbf{v}_j$.

In this paper, we use the weakly-compressible SPH formulation that requires an equation of state such as the Tait's equation

$$P(\rho) = \frac{c_0\rho_0}{7}\left[\left(\frac{\rho}{\rho_0}\right)^7 - 1\right], \quad \text{(A7)}$$

where c_0 and ρ_0 are, respectively, the sound speed and density at zero stress.

A2. Coarse-Grained Molecular Dynamics (CGMD) / Mass-spring modelling (MSM)

In classical mechanics particles move according to the equation

$$m_i \frac{d\mathbf{v}_i}{dt} = -\frac{\partial U}{\partial \mathbf{r}}, \quad \text{(A8)}$$

where U is the total potential. In classical Molecular Dynamics (MD), eq. A8 still applies, but, instead of particles, we calculate the trajectories of atoms or molecules. In this case, U is usually divided in two parts: the non-bonded potential and the intramolecular potential. In our case, the intramolecular potential can be divided further in two subgroups: the bond potential and the angle potentials

$$U_{intramolecular} = U_{bond} + U_{angle}. \quad \text{(A9)}$$

There are various expressions available for both U_{bond} and U_{angle}. In this work, we use the non-linear bond potential

$$U_{bond} = \frac{k_b(r-r_0)^2}{[r_{max}^2-(r-r_0)^2]}, \quad \text{(A10)}$$

where k_b is the Hookean coefficient, r_0 the equilibrium distance, and $r_{\max}$ the maximum extension of the spring, and the harmonic angle potential

$$U_{angle} = k_a(\theta-\theta_0)^2, \quad \text{(A11)}$$

where k_a is an angular Hookean coefficient and θ_0 the equilibrium angle,

Equations (A9─A11) are the basis for the ball-and-stick representation of molecules that can be coarse-grained to model macroscopic solids. This approach can be employed to model macroscopic phenomena such as stretching and bending of solids under the effect of external forces. In the case under investigation, we divide the membrane in a certain number of notional particles and use the potentials of eq. A10 and A11 to simulate its deformation. Figure 1b shows how bond and angle potentials are used in our intestine model. This component of the DMHS has been indicated sometimes as CGMD and sometimes as MSM. The mathematical formulation is the same: at small scales (e.g. microfluidic applications) the term CGMD is preferred (e.g. Alexiadis 2015) at larger scales the term MSM (e.g. Ariane 2016) is preferred.

A3. Coupling the two models

The link between the solid (CGMD particles) and the liquid (SPH particles) is established by the boundary conditions. In continuum mechanics, these conditions are often represented as (Müller et al. 2004)

$$\left(\frac{\partial}{\partial t}\mathbf{u} - \mathbf{v}\right) \cdot \mathbf{n} = 0 \ (\text{no} - \text{penetration}), \tag{A12}$$

$$\left(\frac{\partial}{\partial t}\mathbf{u} - \mathbf{v}\right) \times \mathbf{n} = 0 \ (\text{no} - \text{slip}) \tag{A13}$$

and

$$\sigma_s \mathbf{n} = \sigma_f(-\mathbf{n}) \ (\text{continuity} - \text{of} - \text{stresses}) \tag{A14}$$

where **n** is the normal to the boundary, **u** the displacement of the solid, **v** the velocity of the liquid, σ_s the stresses in the solid and σ_f in the fluid.

In our case, these conditions must be expressed in the particle framework. No-penetration conditions are implemented by a repulsive force such as

$$f(r) = K\left[\left(\frac{r^*}{r}\right)^4 - \left(\frac{r^*}{r}\right)^2\right]\frac{\mathbf{r}}{r^2}, \tag{A15}$$

where r^* is a repulsive radius and K a constant. No-slip conditions can be achieved by superimposing a fluid ghost particle above the solid particles at the interface, while the continuity-of-stress condition is automatically satisfied by eq. A5.

A5. Model parameters

There are two types of parameter required for the simulations: model parameters and simulation parameters. Here we list the numerical values used in the model parameters (simulation parameters are discussed in Section 3.1).

The number of SPH particles used in the simulation is 19,928, 32,756, 42,344, and 59,928 for respectively L = 0.46, 0.81, 1.11, and 1.57 cm. The number of CGMD particles is 5,250. The mass of each particle is $m = 6.13 \cdot 10^{-5}$ kg, the initial distance among particles $\Delta r = 2.5 \cdot 10^{-4}$ m, the smoothing length $h = 2.5 \cdot 10^{-4}$ m and the time step $\Delta t = 10^{-5}$ s. The function W is the so-called Lucy kernel (Liu and Liu 2003). The parameters in eq. A7 are $\rho_0 = 1000$ kg m^{-3} and $c_0 = 1$ m s^{-1}. The parameters in eq. A10 are $k_b = 10^{-4}$ J, $r_0 = 2.5 \cdot 10^{-4}$ m, $r_{max} = 4.5 \cdot 10^{-4}$ m. The parameters in eq. A11 are $k_a = 8 \cdot 10^{-5}$ J, $\theta_0 = \pi/2$ rad. The parameters in eq. A15 are $K = 10^{-10}$ J, $r^* = 2.5 \cdot 10^{-4}$ m.

References

Alexiadis A. (2014) A smoothed particle hydrodynamics and coarse-grained molecular dynamics hybrid technique for modelling elastic particles and breakable capsules under various flow conditions. *Int J Num Meth Eng*; 100:713–719.

Alexiadis A., (2015a) The Discrete Multi-Hybrid System for the simulation of solid-liquid flows *PLoS ONE* 10(5): e0124678

Alexiadis A. (2015b) A new framework for modelling the dynamics and the breakage of capsules, vesicles and cells in fluid flow, *Procedia UTAM* **16**:80−88.

Alexiadis A., Lockerby D.A., Borg M.K. and Reese J.M. (2013), A Laplacian-based algorithm for non-isothermal atomistic-continuum hybrid simulation of micro and nano-flows, *Comput Method Appl M*, **264**:81−94

Alexiadis A., Lockerby D.A., Borg M.K. and Reese J.M. (2014), The atomistic-continuum hybrid taxonomy and the hybrid-hybrid approach, *Int J Num Meth Eng* **98**: 534−546

Alexiadis A., Lockerby D.A., Borg M.K. and Reese J.M. (2015) A particle-continuum hybrid framework for transport phenomena and chemical reactions in multi-component systems at the micro and nano-scale *J Heat Transfer* **137**: HT-14-1130

Ariane M., Alexiadis A., Barigou M., Smoothed Particle Hydrodynamic modelling of an aortic valve with flexible leaflets, *ChemEngDay 2016*, April 2016, Bath United Kingdom

Cook I.J., Furukawa Y., Panagopoulos V., Collins P.J., Dent J.(2000) Relationships between spatial patterns of colonic pressure and individual movements of content *Am. J. Physiol. Gastrointest. Liver Physiol.* **278**:G329–G341.

Dinning, P. G., Wiklendt, L., Maslen, L., Gibbins, I., Patton, V., Arkwright, J. W., Lubowski, D. Z., O'Grady, G., Bampton, P. A., Brookes, S. J., and Costa, M. (2014). Quantification of in vivo colonic motor patterns in healthy humans before and after a meal revealed by high-resolution fiber-optic manometry. *Neurogastroenterol Motil* **26**:1443−1457.

Dinning P.G., Szczesniak M.M., Cook I.J.(2008) Proximal colonic propagating pressure waves sequences and their relationship with movements of content in the proximal human colon *Neurogastroenterol Motil* **20**:512–520

Hur, S. J., Lim, B. O., Decker, E. A., McClements, D. J. (2011). In vitro human digestion models for food applications. *Food Chemistry* **125**:1–12.

Ganzenmüller G. C., Steinhauser M. O., Van Liedekerke P., Leuven K. U. (2011) The implementation of Smooth Particle Hydrodynamics in LAMMPS, Retrieved from lammps.sandia.gov/doc/PDF/SPH_LAMMPS_userguide.pdf (last accessed 03/12/16).

Guerra, A., Etienne-Mesmin, L., Livrelli, V., Denis, S., Blanquet-Diot, S., Alric, M. (2012). Relevance and challenges in modeling human gastric and small intestinal digestion. *Trends biotechnol* **30**:591–600.

Liu GR, Liu MB. (2003) *Smoothed Particle Hydrodynamics: A Meshfree Particle Method.* Singapore: World Scientific Publishing.

Misra J.C., Pandey S.K. (2006) Peristaltic transport of physiological fluids, J.C. Misra (Ed.), Biomathematics: Modeling and Simulation, World Scientific (2006) pp. 177–189

Morris J.P., Fox P.J., Zhu Y. (1997) Modeling Low Reynolds Incompressible Flows Using SPH. *J Comput Phys* **136**:214−226.

Müller M., Schirm S., Teschner M., Heidelberger B., Gross M. (2004) Interaction of fluids with deformable solids. *Comp Animat Virt W* **15**:159−171

Plimpton S. (1995), Fast Parallel Algorithms for Short-Range Molecular Dynamics, *J Comp Phys* **117**:1-19.

Regner M., Östergren K., Trägårdh C. (2008) Influence of viscosity ratio on the mixing process in a static mixer: Numerical study Ind. Eng. Chem. Res. **47**:3030−3036

Sinnott M.D., Cleary P.W, Arkwright J.W, Dinning P.G.(2012) Investigating the relationships between peristaltic contraction and fluid transport in the human colon using Smoothed Particle Hydrodynamics *Comput Biol Med.* **42**:492−503.

Schiller, C., Frohlich, C.P., Giessmann, T., Siegmund, W., Monnikes, H., Hosten, N., Weitschies, W. (2005) Intestinal fluid volumes and transit of dosage forms as assessed by magnetic resonance imaging. *Aliment Pharmacol Ther* **22**:971−979.

Stamatopoulos K., Batchelor H.K., Alberini F., Ramsay J., Simmons M.J. (2015) Understanding the impact of media viscosity on dissolution of a highly water soluble drug within a USP 2 mini vessel dissolution apparatus using an optical planar induced fluorescence (PLIF) method, *Int J Pharm* **495**:362-73.

Stamatopoulos K., Batchelor H.K., Simmons M.J. (2016) Dissolution profile of theophylline modified release tablets, using a biorelevant Dynamic 3 Colon Model, *Eur. J. Pharm. Biopharm.* (accepted)

Tables

sub-period \ pocket	0	1	2	3	4	…	N
0	0	0	0	0	0	…	0
t_w	1	-1	0	0	0	…	0
2 t_w	1	0	0	0	0	…	0
3 t_w	0	1	-1	0	0	…	0
4 t_w	0	1	0	0	0	…	0
5 t_w	0	0	1	-1	0	…	0
6 t_w	0	0	1	0	0	…	0
…	…	…	…	…	…	…	…
(2N+5) t_w	0	0	0	0	0	…	1

Table 1. Matrix representation of the peristaltic dynamics. Each t_w is a 'sub-period', four sub-periods from a 'haustrum period', (2N+5) t_w sub-periods form a 'peristaltic-period'.

	k=0	k=1	k=2	k=3
j=0	n_P	0	0	0
j=1	$(1-\alpha)n_P$	αn_P	0	0
j=2	$(1-\alpha)n_P$	$\alpha(1-\alpha)n_P$	$\alpha^2 n_P$	0
j=3	$(1-\alpha)n_P$	$\alpha(1-\alpha)n_P$	$\alpha^2(1-\alpha)n_P$	$\alpha^3 n_P$

Table 2. Number of particles in the first 4 pockets during the first 3 haustrum-periods (pouring mode)

sub-period \ pocket	0	1	2	3	4	…	N
0	0	0	0	0	0	0	…
t_w	1	-1	0	0	0	0	…
2 t_w	1	0	0	0	0	0	…
3 t_w	**1**	1	-1	0	0	0	…
4 t_w	**1**	1	0	0	0	0	…
5 t_w	**1**	**1**	1	-1	0	0	…
6 t_w	0	**1**	1	0	0	0	…
7 t_w	0	**1**	**1**	1	-1	0	…
8 t_w	0	0	**1**	1	0	0	…
9 t_w	0	0	**1**	**1**	1	-1	…
…	…	…	…	…	…	…	…

Table 3. Matrix representation of the new peristaltic wave. The differences between the old and new wave are in bold.

Figures

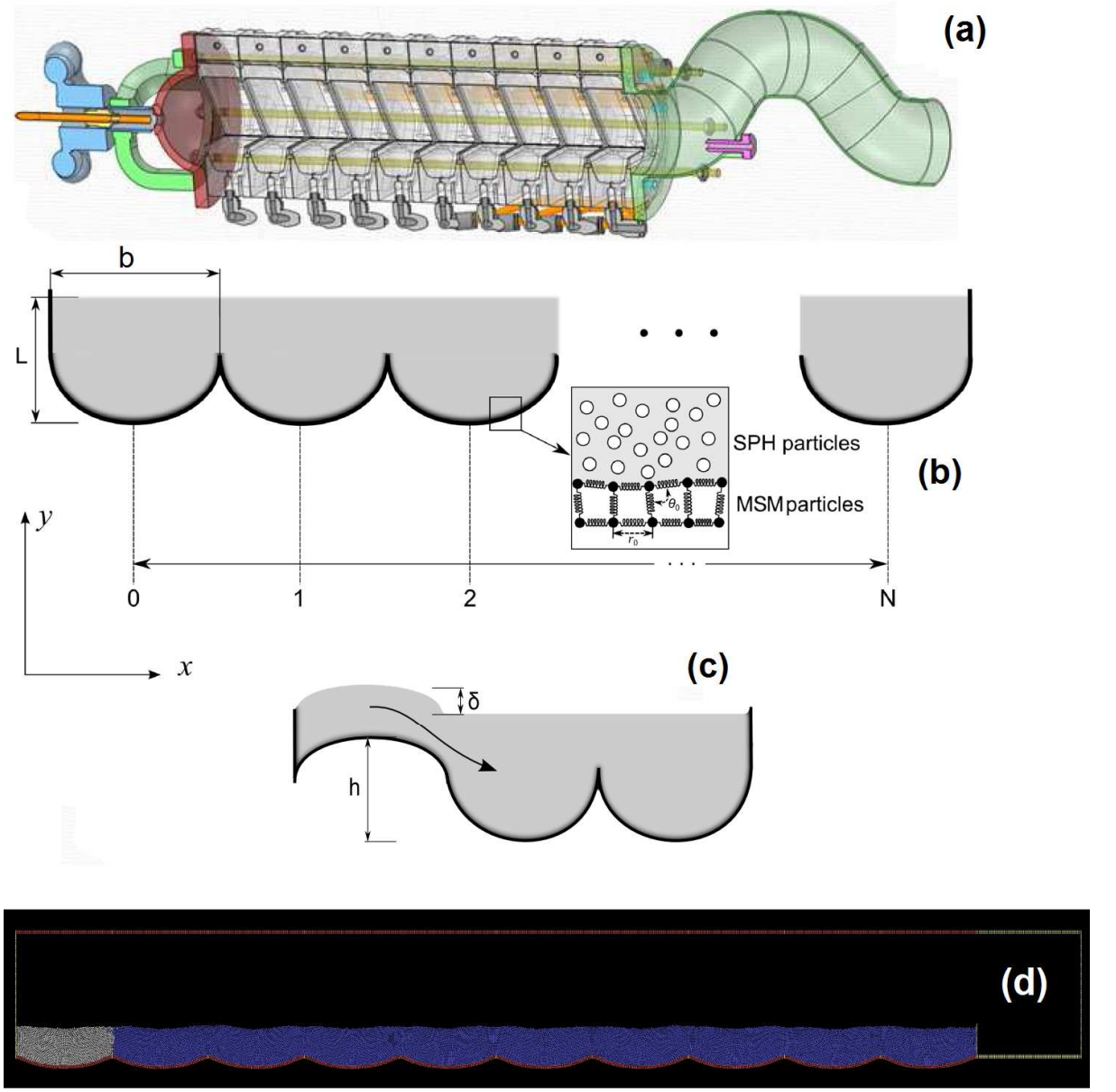

Figure 1. Artificial colon model used in the experiments (a), geometry used in the simulation (b), contraction of the pocket's membrane (c), and simulation's snapshot at *t* = 0 (d).

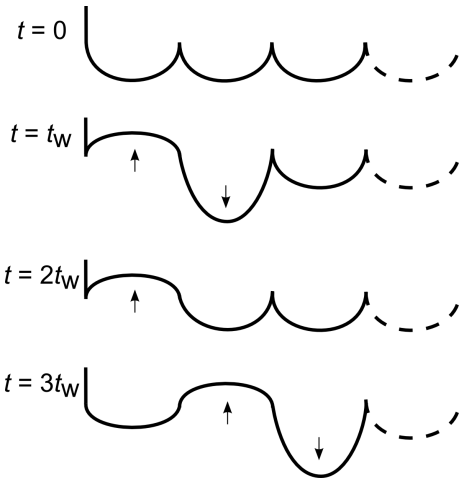

Figure 2. Contractions and expansion of the membrane sections during the peristaltic wave.

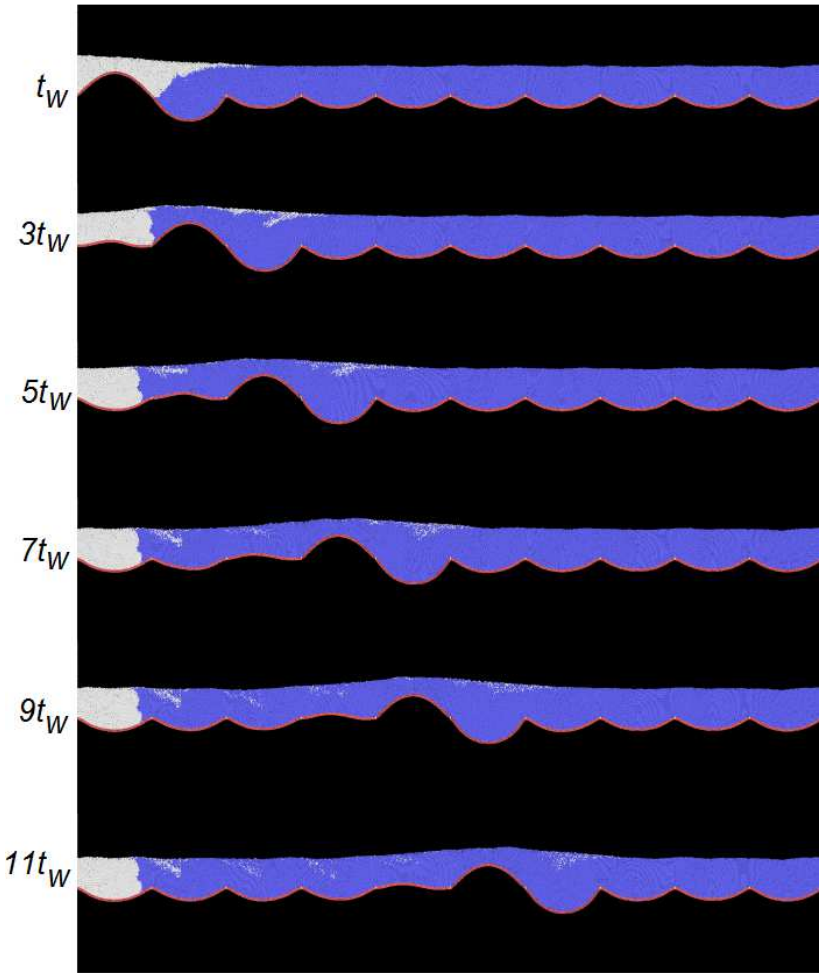

Figure 3. Simulation snapshots illustrating the fluid motion induced by a peristaltic wave for $\nu = 10^{-6}$ m^2 s^{-1}, $L = 1.11$ cm and $V_w = 1.45$ cm s^{-1}. The tracking (white) particles partially mix with the fluid of other pockets (pouring mode) and partially advance on the surface of the channel (surfing mode). The fluid that moved in the second pocket at t_w partially flows back into the first pocket at $3t_w$ (ineffective surfing). See Section 4 for details on these three propagation modes.

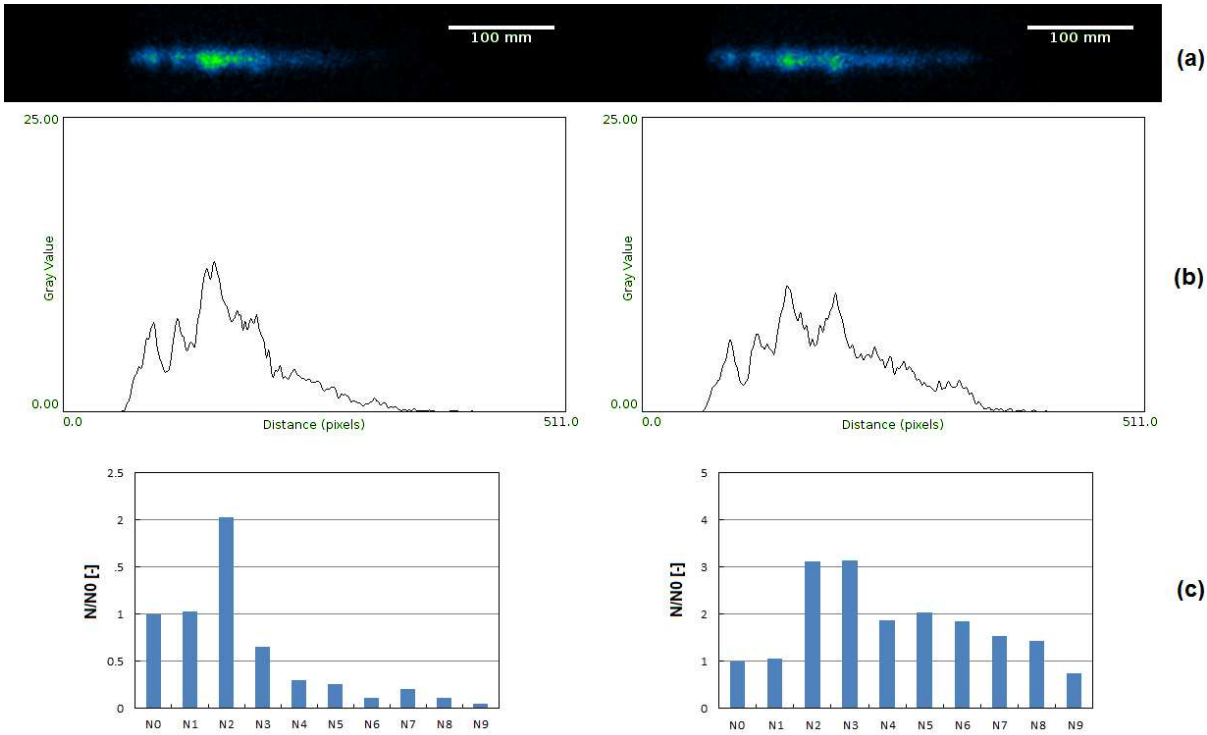

Figure 4. PET images: experimental snapshots (a) and greyscale distribution plots (b), compared to dimensionless concentration N/N0 of tracker particles in the simulations (c) after 5 and 7 peristaltic waves ($\nu = 10^{-6}$ m^2 s^{-1}, $L = 0.8$ cm, $V_w = 1.45$ cm s^{-1}). The concentration N0 in the first pocket has been normalized to match the experiments and the distribution rescaled accordingly. Units between (b) and (c) are different: distributions (b) are continuous and indicate the tracer concentration along the whole channel; distributions (c) are discrete and indicate the concentration of white particles in each pocket.

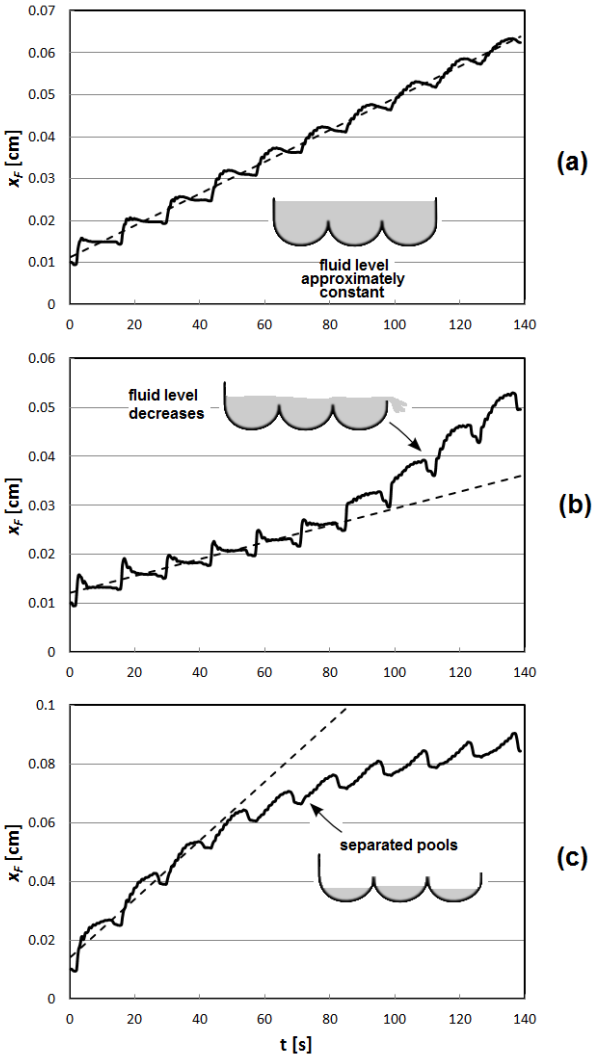

Figure 5. Front penetration x_F versus time for: (a) L= 0.46 cm $\nu = 2 \cdot 10^{-6}$ m^2 s^{-1}, V_w = 1.45 cm s^{-1}, (b) L= 0.81 cm $\nu = 1.6 \cdot 10^{-6}$ m^2 s^{-1}, V_w= 1.45 cm s^{-1}, (c) L= 0.46 cm $\nu = 10^{-6}$ m^2 s^{-1}, V_w= 1.45 cm s^{-1}

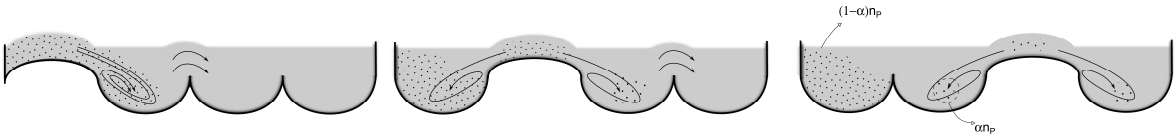

Figure 6. Pouring mode

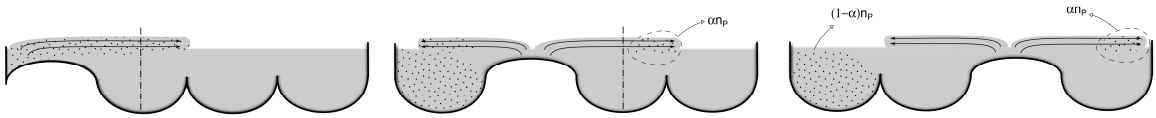

Figure 7. Surfing mode

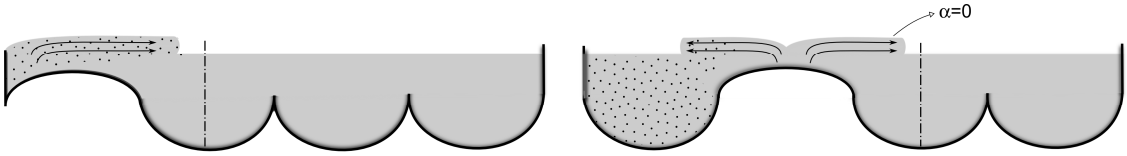

Figure 8. Ineffective surfing

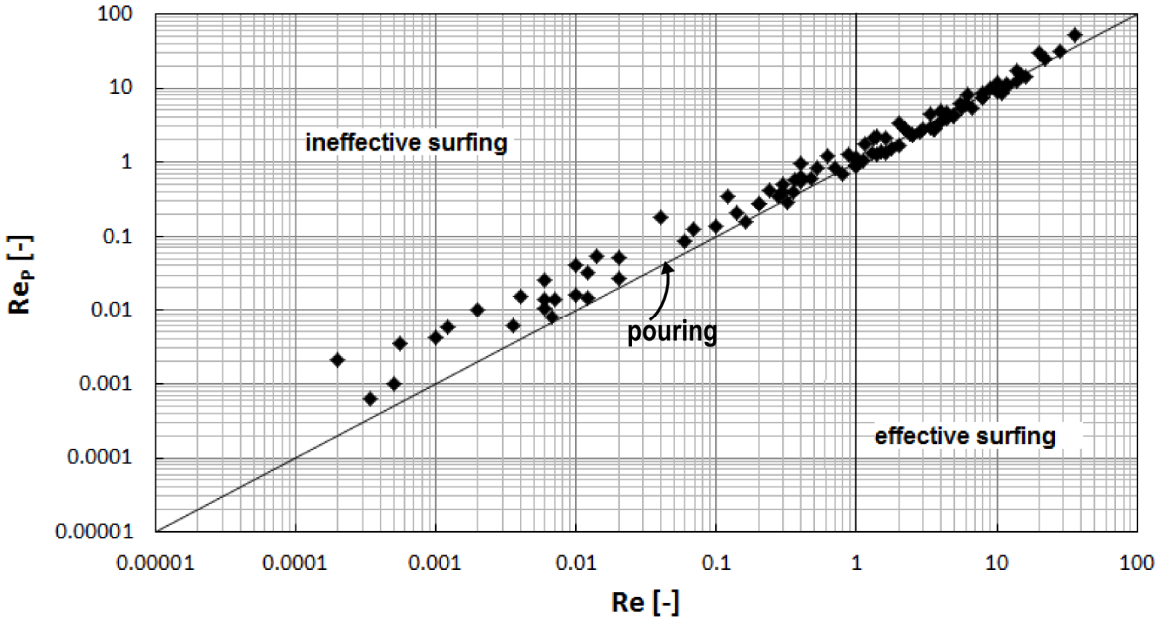

Figure 9. Reynolds number calculated using u_F (Re) versus Reynolds number calculated using u_P (Re_P).

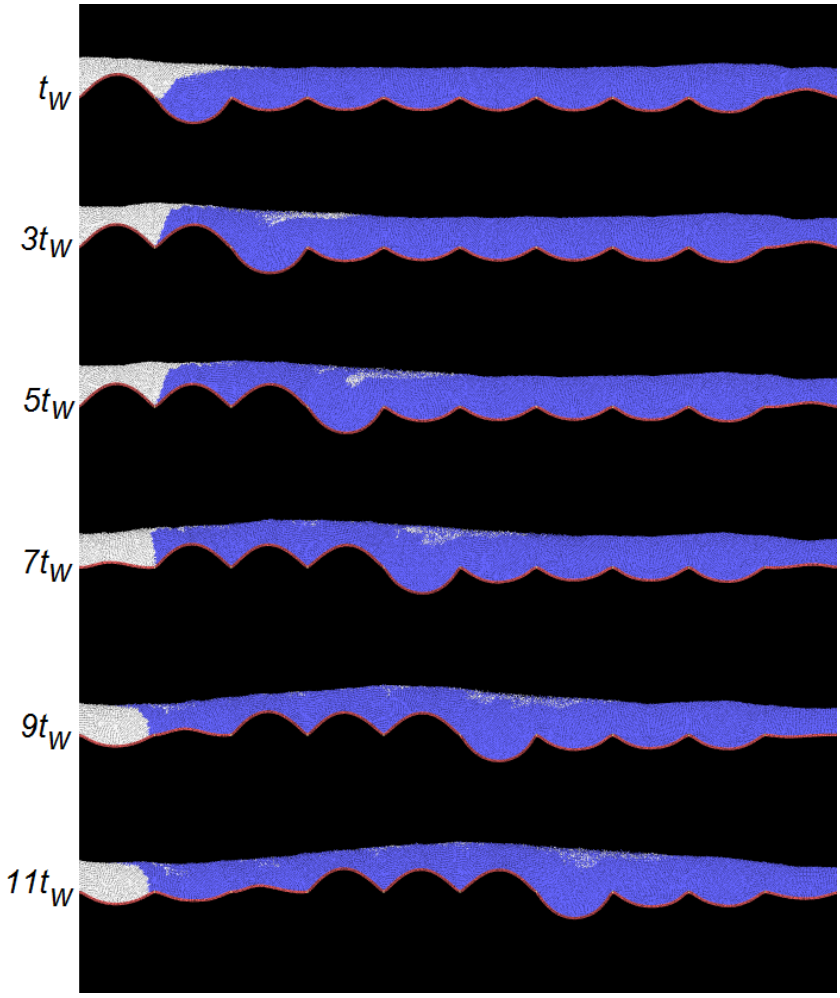

Figure 10. Simulation snapshots of the new peristaltic wave ($\nu = 10^{-6}$ m^2 s^{-1} and L = 1.11 cm).

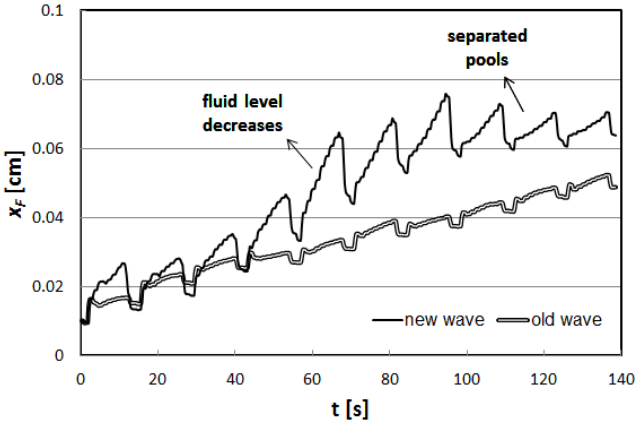

Figure 11. Front propagation in the case of $\nu = 10^{-6}$ m^2 s^{-1} and L = 1.11 cm: old wave versus new wave.

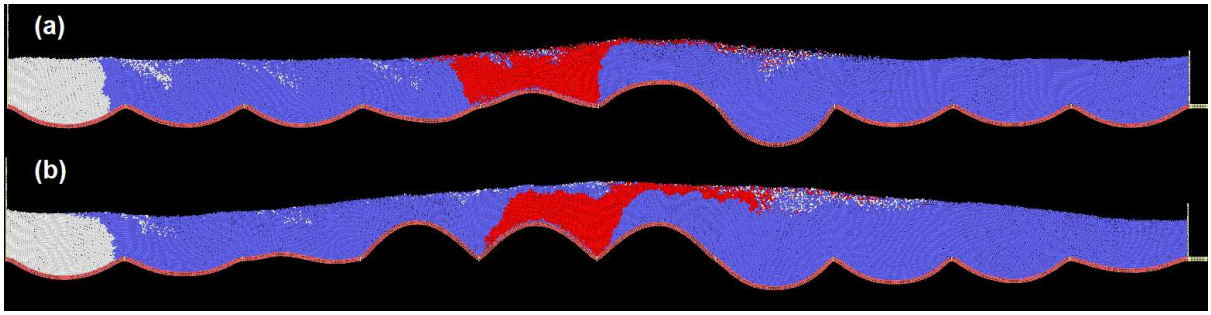

Figure 12. Propagation of tracking particles from the first and fifth pockets in the case of $\nu = 10^{-6}$ m^2 s^{-1} and L = 1.11 cm, observed when the peristaltic wave crosses the fifth pocket: old wave (a) versus new wave (b).

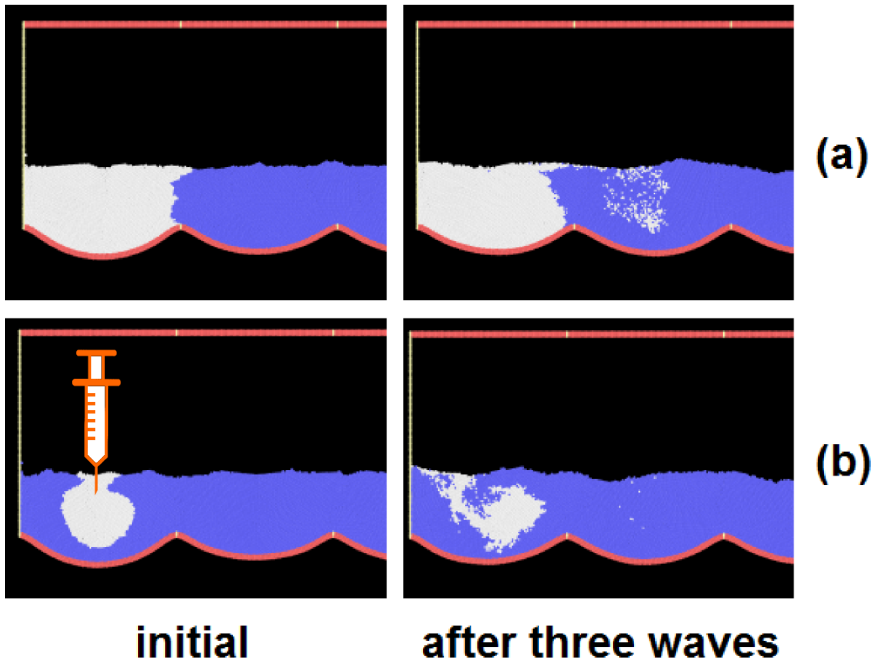

Figure 13. Screenshots at the beginning of the simulation and after three peristaltic waves: (a) tracer and fluid with same viscosity ($500 \cdot 10^{-6}$ m^2 s^{-1}), (b) tracer and fluid with different viscosities (fluid $500 \cdot 10^{-6}$ m^2 s^{-1}, tracer 10^{-6} m^2 s^{-1}).